Turkish Journal of Electrical Engineering & Computer Sciences

http://journals.tubitak.gov.tr/elektrik/

Research Article

Turk J Elec Eng & Comp Sci
(2017) 25: 4510 – 4521

doi:10.3906/elk-1701-312

Development and experimental evaluation of a 3D ultra-wideband localization system

Ali MUQAIBEL*
Department of Electrical Engineering, King Fahd University of Petroleum & Minerals (KFUPM), Dhahran, Saudi Arabia

Received: 30.01.2017 • **Accepted/Published Online:** 24.07.2017 • **Final Version:** 03.12.2017

Abstract: In this paper, an ultra-wideband (UWB) synthetic aperture radar system that can perform 3D localization of objects is implemented. The system consists of a moving platform that positions two UWB horn antennas. The 3D image construction is performed using the delay-sum beamforming algorithm. Experiments were performed using two data acquisition techniques, namely, background measurements technique and change detection. The former can be used for imaging stationary targets while the latter is applicable for moving objects. At different distances and orientations from the antennas, various targets were imaged. Through-wall imaging was also considered. The system is augmented with a graphical user interface that allows the user to change input parameters and display a 3D image of the target along with plots of frequency and time analysis at different antenna positions. The results demonstrate the system applicability for many indoor applications.

Key words: Localization, radar imaging, through wall imaging, ultra-wideband, synthetic aperture radar

1. Introduction

Ultra-wideband (UWB) synthetic aperture radar (SAR) systems have day- and night-imaging capabilities and support numerous applications in many fields, such as through-wall human detection to locate survivors during natural disasters or terror attacks [1]. SAR imaging systems have many medical applications, like heartbeat monitoring and detection of cancer and cardiovascular diseases [2]. They also have military applications like minefield detection, and other applications related to the oil industry and subearth imaging [3]. Industrial applications like real-time tracking of materials, equipment, and personnel, as well as safety management are demonstrated in [4]. In SAR systems, the motion of the antennas over a certain region creates a large "synthetic" antenna aperture [5]. This results in a better resolution than conventional radars. UWB systems are used to ensure suitable wall penetration along with high resolution for object detection.

There have been earlier publications on 3D UWB SAR imaging with emphasis on human detection. The Center for Advanced Communications at Villanova University has conducted several through-the-wall imaging (TWRI) experiments and collected data on different settings. Three different scenes were considered: an empty scene, a calibration scene, and a populated scene. A jug of saline solution was used to crudely approximate a human [6,7]. Kidera et al. performed some experiments to verify their improved signal processing techniques for 3D imaging with impulse radar [8]. The work was extended for TWRI applications in [9]. They relied on the envelope of modified spheres method combined with spectrum-offset correction. The single processing

*Correspondence: muqaibel@kfupm.edu.sa

was further improved by combining reference signal optimization with Capon to enhance the resolution. The algorithm was applied to experimental imaging of metallic targets with sharp edges [10].

The authors in [1] presented 3D imaging results for some TWRI experiments using a human mock-up target wrapped with a strong metallic reflector. The resolution is limited by the 2 to 3 GHz bandwidth used. Additional 3D imaging with a human mock-up target was done by [11] at two frequency ranges, from 2 to 4 GHz and from 8 to 10 GHz. The second band was used for higher resolution but for low-loss obstructions. An extended frequency range of 5 to 25 GHz was used by [12] to obtain a focused 3D image with efficient fast processing using deconvolution. However, the method is only applicable to small objects, such as concealed weapons, and the experimental verification was performed in an extremely controlled environment, replacing the human target with a conductive dummy. Some basic 3D experiments with real human targets are presented in [13]. However, the experiment was performed with very limited bandwidth of 0.5 to 1 GHz in a controlled chamber. Results for UHF UWB SAR for airborne detection of moving humans in foliage are presented in [14].

The authors in [15] focused on detecting human targets in a ruin scene using impulse radio with a 400 MHz bandwidth. Wavelet transformation was proposed and compared with the conventional power spectrum density-based algorithm. The work in [16] and the cited references therein concentrate on the detection of human respiration in ruins. A novel UWB linear array was used to obtain vital sign features, including azimuth, range, and respiration frequency. The method was verified experimentally using artificial ruins in which one person was trapped. The UWB signal had a spectrum from 0.5 to 1.5 GHz.

Moving targets in the near-field were addressed in [17]. The computationally intensive processing involves generating multiple images assuming different target speeds and then finding the most focused image. Both simulated and measured data for a mannequin and a handgun were used to demonstrate the imaging capability and associated computational complexity. The authors in [18] addressed the impact of the environment on the detection of walking humans. They performed experiments using a frequency range from 1 to 3 GHz in a semianechoic chamber environment and open office space. Compared with impulse radio, M-sequence UWB radar was better suited for detecting static human targets in larger distances [19]. Signal processing needed for human tracking is discussed in [20]. A UWB signal with 1 GHz center frequency was processed using the local mean decomposition method to extract signatures of human motion [21]. The simpler problem of localizing moving humans with an active wearable UWB antenna is addressed in [22]. Locating humans with active antennae has applications in healthcare, sports, and well-being. Other high-accuracy 3D UWB radar imaging experiments are available, but are usually for deterministic objects with homogeneous material and well-defined shapes [23].

Based on the literature review and due to the importance of the supported applications, there is a need for more realistic human experiments with different frequency bands and measurement parameters. This paper presents a high-resolution UWB 3D SAR localization and imaging system. The system consists of a moving platform combining UWB antennas controlled by a computer. The system is used to produce 3D images of different targets by acquiring data from various positions. Moreover, a graphical user interface (GUI) is developed to automate the process. In order to isolate the target to be imaged and eliminate other objects in the scene, two imaging techniques are used. The first technique is based on background measurements technique (BMT), which is applicable for stationary targets. The second technique is referred to as change detection (CD), which can be used for imaging moving objects. Even if the person is stationary, heartbeat and lung motion change the phase and amplitude of the reflected wave.

Compared with other published results, the developed system is unique in terms of its bandwidth with

results using real humans in real environments. It is worth noting that the Doppler system developed by Saho et al. in [1] and the publications that follow is different from the presented work in many aspects. They assumed a specific target, like a pedestrian, and made all the necessary assumptions related to size and speed. In some cases, a treadmill was used for velocity control; in some other cases, the movement was not casual and made to maximize the Doppler, as slow and nonmoving targets are difficult to identify. Absorbers were also used, which makes the environment somewhat controlled rather than being fully realistic. This work augments the published results and provides a means to cooperate with other researchers, as the data and details of the experiments will be available for comparison and future enhancement. Additional assumptions, calibrations, and associated filtering will always result in better imaging.

The paper is organized as follows: an overview of the system and components followed by the system operation is presented in Section 2. The 3D imaging algorithm is explained in Section 3. Section 4 presents imaging results using BMT and CD. Finally, Section 5 concludes the paper.

2. System overview and operation

Three-dimensional imaging requires collecting data along a 2D plane and then processing these data by image construction algorithm. A moving platform was constructed as shown in Figure 1. The platform controller receives commands from a personal computer (PC) through a Bluetooth connection. The complete system consisted of three main subsystems, namely, microwave, mechanical, and controlling subsystems.

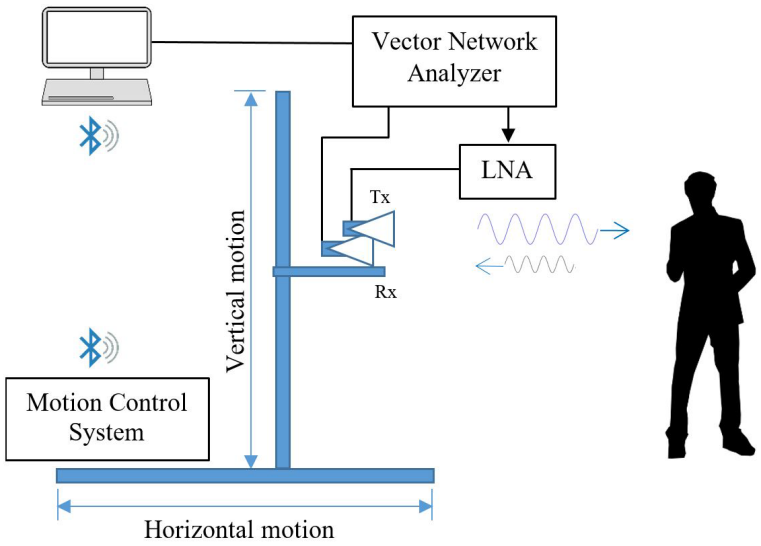

Figure 1. Side-view of the imaging system.

The vector network analyzer (VNA) (Agilent 8510C; Santa Clara, CA, USA) sends stepped frequency continuous wave signals with a frequency ranging from 50 MHz up to 10 GHz. Then the VNA receives the reflected signals and measures their amplitude and phase and stores them as a complex vector to be transferred to the PC. In order to extend the range, a low-noise amplifier was used at the transmitter side. Placing the amplifier at the receiver port would amplify more noise and risk the input port of the VNA. The unidirectional low-noise amplifier (A-INFO LA1018N3209) works at an optimal range of frequencies from 1 GHz to 18 GHz, supporting a gain of 28 to 36 dB.

A bistatic two-port configuration was used and S_{21} parameters were measured. For high-resolution

imaging, a UWB horn antenna (A-INFO LB-10180), which can support frequencies from 1 GHz to 18 GHz with linear polarization, was used. Wideband coaxial cables were used to interconnect the system.

To get different aspect angles, the mechanical subsystem consisted of a platform that can move in x, y, and z directions, as shown in Figure 2. The platform moved using three stepper motors attached to screw threads. Stepper motors provided a large range of torque and provided a self-locking feature. The accuracy in the antenna positioning is critical and important for precise imaging. Each of the three motors requires 500 steps to finish one complete revolution. Although the platform has precise, accurate, and stable motion, it has some limitations related to the maximum dimension and speed.

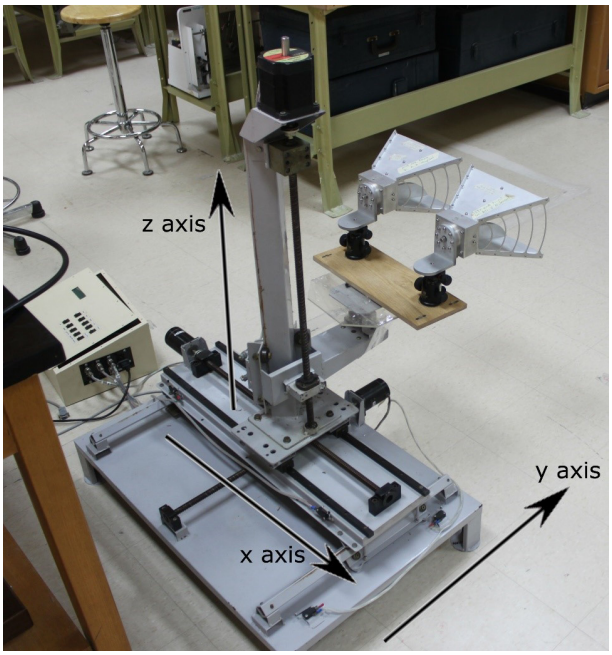

Figure 2. Developed moving antenna platform.

The control subsystem panel is designed to be programmed by MATLAB. An Arduino microcontroller was connected to a Bluetooth chip to receive commands from the PC in order to control the motors' driving circuits. The stepper motor requires a fixed driving current and a specific sequence of operation across the motor windings to control the speed and direction of rotation. This is achieved by using Super VEXTA 5-Phase Driver that was interfaced with the microcontroller. In addition, six limit switches were connected for safe operation.

Parameters such as the starting frequency, the frequency step, and the end frequency, in addition to the maximum and minimum horizontal and vertical positions of the antennas in the platform, could all be adjusted through the GUI. After measuring the complex data reflected at all positions, the image construction algorithm was executed.

3. Image construction

The image construction algorithm utilizes the delay-sum beamforming (DSBF) algorithm [24], which generates a 3D intensity matrix at each antenna position and multiplies all matrices to generate a total intensity matrix that is translated to an image.

3.1. Data acquisition

For the BMT, a background scan covering the support of the target without the target in place is performed. After that, the target is placed in position and another scan is conducted. The difference between the two readings is used as an input to the imaging algorithm. Background measurements are not possible and one has to use CD. To implement CD, two readings are acquired successively; that is, once the first reading is completed, a second reading is executed at the same antenna position. The difference between the scans is used as an input to the imaging algorithm.

3.2. DSBF in 3D

The DSBF algorithm uses the time delay of the received signal from different antenna positions to determine the target position [24]. The transmitted sinusoidal signal, $y_t(t) = A\cos(2\pi ft)$, is reflected back and received via the VNA with time delay t_d. The received signal with amplitude B can be represented as

$$y_r(t) = B\cos\left(2\pi f\left(t - t_d\right)\right) \tag{1}$$

In order to construct an image, the DSBF compares the delay with an expected time delay for each portion of the image. The expected time delay is the theoretical delay calculated for the signal to travel from the antennas to the target and reflect back. After comparing the received signal with the expected time delay, the process is repeated for different transmit and receive antenna positions. Finally, all results are combined in order to get the correlation of all readings.

The calculated two-way distances between the antennas and each voxel, as shown in Figure 3, form the 3D distance matrix. The delay matrix is simply the distance matrix divided by the propagation speed. The delay for each voxel is calculated assuming free space condition with $c = 3 \times 10^8$ m/s.

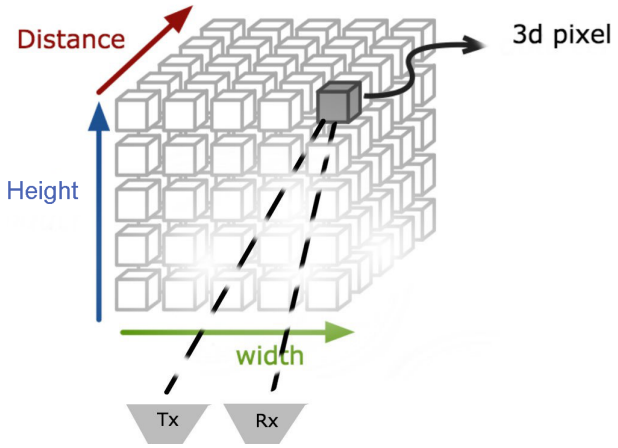

Figure 3. The distance from the transmitting and receiving antennas for each voxel of the image.

In order to determine the position of a target on the 3D image, the calculated expected time delay, $t_{cal}(x, y, z)$, of each voxel located at (x, y, z) is compared with the time-delay, t_d, of the received signal. The comparison is done by multiplying the received signal by $exp(j2\pi ft_{cal})$ as shown below:

$$y(t) = Re\left\{Be^{j2\pi ft}e^{-j2\pi ft_d}e^{j2\pi ft_{cal}}\right\} \tag{2}$$

The voxels of the 3D intensity matrix will have high values if the signal delay matches the expected delay of

each voxel and vice versa. The intensity matrix is expressed as

$$y_{\text{intensity}}(x,\, y,\, z, \alpha,\, \beta) = \begin{cases} \text{high value} & t_{cal} = t_d \\ \text{low value} & t_{cal} \neq t_d \end{cases} \tag{3}$$

The steps are repeated for each antenna position to generate an intensity matrix and then all the intensity matrices are fused in order to get the final results. Image fusion could be additive or multiplicative. Multiplication was used in our case as it gave better results.

$$y_{\text{total intensity}} = \prod_{1}^{i} \prod_{1}^{j} y_{\text{intensity}}(x,\, y,\, z, \alpha_i,\, \beta_j) \tag{4}$$

where α_i and β_j are the horizontal and vertical antenna positions, respectively. Unwanted data that are below a certain threshold value may be eliminated from the intensity matrix.

3.3. Results and analysis

In this section, the experimental results for BMT are presented, followed by the CD and through-wall imaging experiments. The first experiment demonstrates the imaging of a stationary object with BMT. A metal parallelepiped object (with dimensions $0.17 \times 0.09 \times 0.63\, m$) was placed on a chair $2\, m$ away from the SAR system. Figure 4 shows a picture of the metallic object while being scanned. Figure 5 shows the resulting side and 3D views for the image. The antenna positioning matrix in this experiment was of size 8×20; that

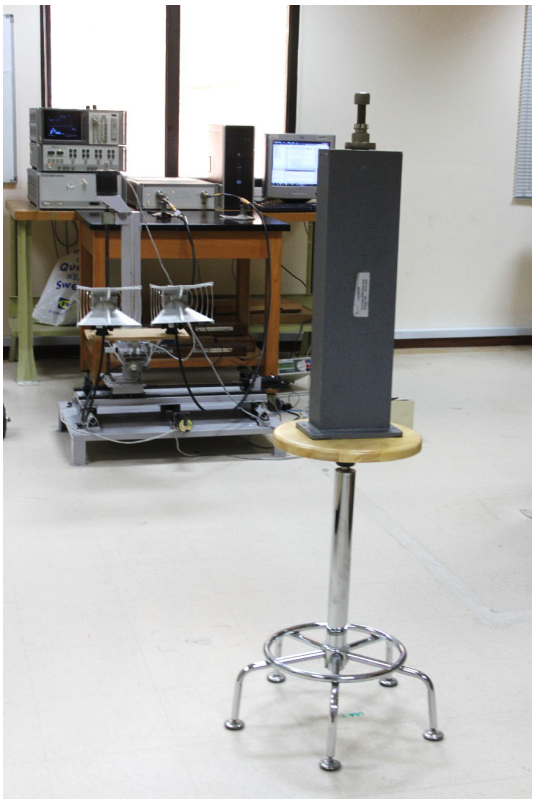

Figure 4. Picture of the waveguide 2 m away from the antennas.

is, 8 vertical levels and 20 horizontal positions. The size of the antenna positioning frame was $1.25 \times 1.18\,m$. Beamforming was implemented with voxel resolution of 1 cm in each dimension. The noise threshold was set to 0.1 of the maximum voxel intensity. The object was located correctly at a distance of $2\,m$ and the height was estimated as $0.6\ m$ compared to $0.63\,m$. The rod extension at the top of the parallelepiped object could be identified. The original width of $0.17\,m$ was estimated as $0.15\,m$. As expected, the front view resolution was higher than the side view because it was along the synthesized aperture.

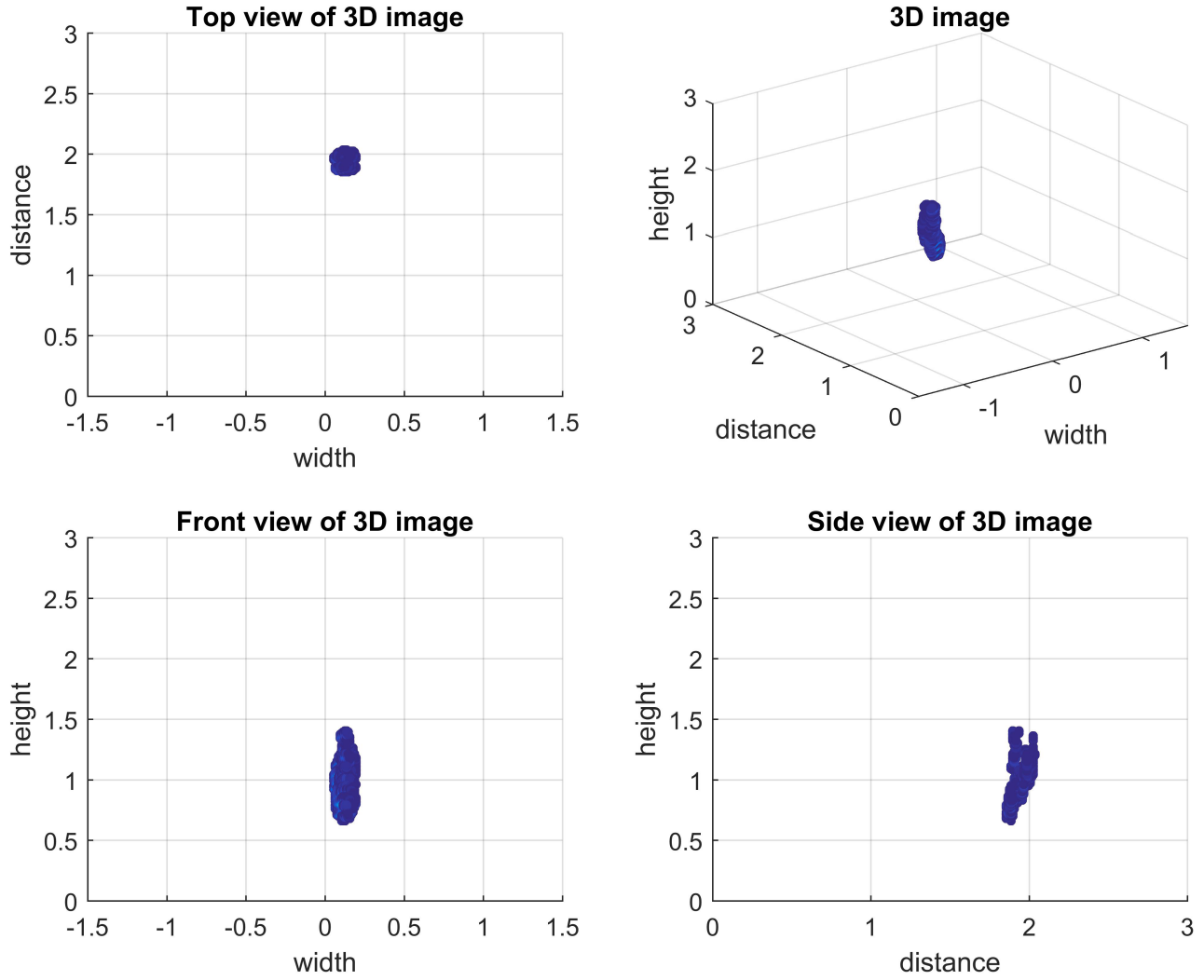

Figure 5. The 3D image and side views of a stationary metal parallelepiped object placed 2 m away from the antennas. All axes are in meters.

In applications related to human radar imaging, it is usually not possible to perform background measurements. In the remaining experiments that scan the human body, CD was used. A human sitting on a chair $3\,m$ away from the antennas was imaged as in Figure 6. The antenna positioning matrix was 8×20. The maximum horizontal displacement of the antennas was 1.25 m, while the vertical displacement was 1.18 m. The results in Figure 7 show that the system estimated the target at a distance of 3 m with a height of 1.5 m, which corresponds to the distance and height of the male target sitting on the laboratory chair. The error in the estimated width of the imaged target is less than 10%. All techniques that depend on CD or Doppler effects

reveal the moving parts of the body rather than the details of the target shape. Hence, the image intensity is high around the chest, hands, and legs, because their movements result in higher change and Doppler compared with other parts of the body.

Figure 6. Picture of human being scanned at 3 m away from the antennas.

The system resolution in the downrange is determined by the transmitted power and bandwidth, while the cross-range resolution is affected by the dimensions of the SAR system, number of antenna positions in the scanning matrix, and the antenna directivity. To study the maximum downrange of the system, other experiments were performed with the person sitting at varying distances away from the SAR system. At 6 m, the system was able to detect and determine the distance of objects. However, the image accuracy went down drastically. Critical parameters that have significant impact on the accuracy are the transmitted power and the dimensions of the antenna positioning frame.

Finally, the SAR system was set to scan through the wall at a distance of 0.3 m from the wall. A team member was sitting on a chair 0.3 m away from the other side of the wall. The thickness of the concrete wall was 0.4 m which means the target was 1 m away from the SAR system. The near-far field distinction is usually made based on the wavelength. When dealing with UWB signals, part of the used band might violate the far-field assumption. Due to the high attenuation caused by the concrete wall and limited transmitted power, the antenna is put at close proximity to the wall, which means that the far-field assumption is traded off for the strength of the signal. Figure 8a depicts the setup while scanning through the wall. Figure 8b shows the result obtained from this experiment. A mismatch between the distance of the object in the image and the actual distance of the human object is caused by the roundtrip delay through the wall.

This delay can be compensated for by estimating the relative permittivity, ε_r, of the wall and its impact on the speed of propagation. Then the delay can be calculated from the speed, given the dimension of the wall. In this experiment, the actual and estimated distance of the body were compared, and the fact that electromagnetic waves travel roughly at the speed of light was used to estimate the relative permittivity of the

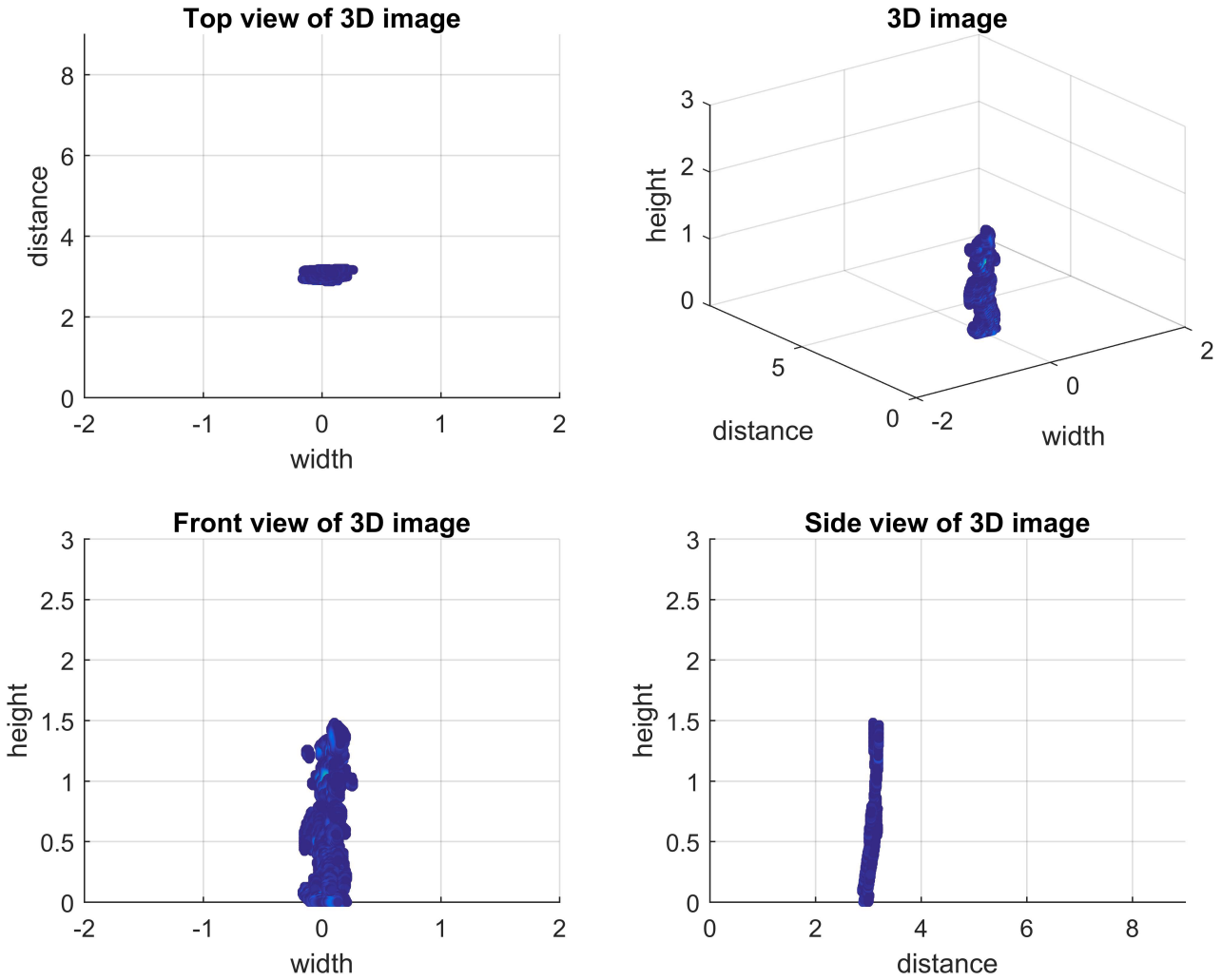

Figure 7. The 3D image and side views as a result of using CD to scan a human body sitting 3 m away from the antennas. All axes are in meters.

wall. The formula used is

$$\frac{\tau}{2}=\frac{0.6}{c}+\frac{0.4\sqrt{\varepsilon_r}}{c} \tag{5}$$

where τ is the roundtrip delay caused by the wall and 0.6 m and 0.4 m are the distances traveled by the waves in the air and in the wall, respectively.

The estimated value of ε_r according to Eq. (5) is in agreement with large range of values reported in the literature [25]. The specific value of the dielectric constant depends on the wall material, shape and moisture content in addition to the frequency of operation. It is possible to develop the image construction algorithm to overcome the distance mismatch issues once the relative permittivity is known. Another major reflection is detected due to the wall location. The system is very robust as the person is not moving, and the detection is a result of change due to breathing and heartbeat.

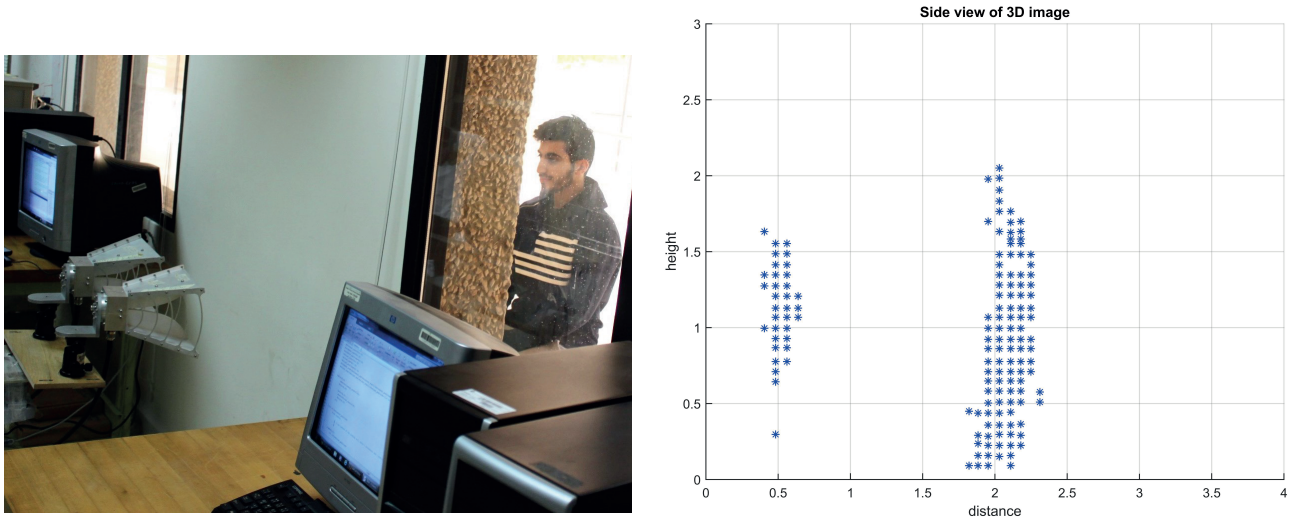

(a) (b)

Figure 8. Through-the-wall imaging a) picture of the setup with human target behind the wall being scanned, b) the reconstructed side view image (all axes are in meters).

4. Conclusion

In this paper, a 3D UWB SAR system with high resolution was implemented and tested. Objects could be imaged in 3D using SAR system that utilizes DSBF algorithm. These images were produced using two techniques: BMT for stationary targets and CD for moving objects. The whole system was wirelessly controlled by a central computer. The system was able to image objects up to 6 m away, which was the maximum distance inside the lab. However, as the distance increases, target dimensions in the image become less accurate. Moreover, through-wall images were produced using CD. An estimate of the wall's relative permittivity was generated with the implemented setup.

For future improvement of the image accuracy, 3D data acquisition could be employed. Moreover, another image construction algorithm could be used instead of DSBF, such as the compressive sensing algorithms. Such algorithms outperform DSBF in image quality and processing [24].

Acknowledgment

This work is funded by the National Plan for Science, Technology and Innovation (Maarifah)-King AbdulAziz City for Technology through the Science and Technology Unit at King Fahd University of Petroleum and Minerals (KFUPM), Kingdom of Saudi Arabia, award number 15-ELE4651-04. The author would like to acknowledge the help provided by his students in performing the experiments and data collection.

References

[1] Saho K, Sakamoto T, Sato T, Inoue K, Fukuda T. Experimental study of real-time human imaging using UWB Doppler radar interferometry. In: 6th European Conference on Antennas and Propagation; 26–30 March 2012; Prague, Czech Republic. New York, NY, USA: IEEE. pp. 3495-3499.

[2] Brovoll S, Berger T, Paichard Y, Aardal O, Lande TS, Hamran SE. Time-lapse imaging of human heartbeats using UWB radar. In: IEEE 2013 Biomedical Circuits and Systems Conference; 31 October–2 November 2013; Rotterdam, the Netherlands. New York, NY, USA: IEEE. pp. 142-145.

[3] Oloumi D, Pettersson M, Mousavi P, Rambabu K. Imaging of oil-well perforations using UWB synthetic aperture radar. IEEE T Geosci Remote 2015; 53: 4510-4519.

[4] Silva B, Pang Z, Akerberg J, Neander J, Hancke G. Experimental study of UWB-based high precision localization for industrial applications. In: IEEE International Conference on Ultra-Wideband; 1–3 September 2014; Paris, France. New York, NY, USA: IEEE. pp. 280-285.

[5] Chan Y, Koo V. An introduction to synthetic aperture radar (SAR). Prog Eelectromagn Res B 2008; 2: 27-60.

[6] Ahmad F, Amin MG. Through-the-wall radar imaging experiments. In: IEEE 2007 Workshop on Signal Processing Applications for Public Security and Forensics; 11–13 April 2007; Washington, DC, USA. New York, NY, USA: IEEE. pp. 1-5.

[7] Dilsavor R, Ailes W, Rush P, Ahmad F, Keichel W, Titi G, Amin M. Experiments on wideband through the wall imaging. In: SPIE Symposium on Defense and Security, Algorithms for Synthetic Aperture Radar Imagery XII Conference; 19 May 2005; Orlando, FL, USA. Bellingham, WA, USA: SPIE. pp. 196-209.

[8] Kidera S, Kani Y, Sakamoto T, Sato T. An experimental study for a high-resolution 3-D imaging algorithm with linear array for UWB Radars. In: IEEE 2007 International Conference on Ultra-Wideband; 24–26 September 2007; Singapore, Singapore. New York, NY, USA: IEEE. pp. 600-605.

[9] Kidera S, Sakamoto T, Sato T. High-resolution 3-D imaging algorithm with an envelope of modified spheres for UWB through-the-wall radars. IEEE T Antenn Propag 2009; 57: 3520-3529.

[10] Kidera S, Sakamoto T, Sato T. Super-resolution UWB radar imaging algorithm based on extended Capon with reference signal optimization. In: the 4th European Conference on Antennas and Propagation (EuCAP); 12–16 April; Barcelona, Spain. Brussels, Belgium: EurAAP AISBL. pp. 100-109.

[11] Wang Y, Fathy AE. Three-dimensional through wall imaging using an UWB SAR. In: IEEE 2010 Antennas and Propagation Society International Symposium; 11–17 July; Toronto, ON, Canada. New York, NY, USA: IEEE. pp. 1-4.

[12] Savelyev TG, Yarovoy A. 3D imaging by fast deconvolution algorithm in short- range UWB radar for concealed weapon detection. Int J Microw Wirel Technol 2013; 5: 381-389.

[13] Zhao Y, Lu B, Sun X. Three-dimensional imaging for UWB through-the-wall radar. In: The 3rd International Conference on Information Science and Technology; 23–25 March 2013; Yangzhou, China. New York, NY, USA: IEEE. pp. 1503-1506.

[14] Thomas K, Anders G, Per-Olov F, Tommy J, Gunnar S, Lars U. Experimental results for human detection in UHF UWB SAR. In: 10th European Conference on Synthetic Aperture Radar; 3–5 June 2014; Berlin, Germany. New York, NY, USA: IEEE. pp. 678-681.

[15] An Q, Li Z, Liang F, Lv H, Chen F, Qi F, Wang J. Wavelet based human target detection in complex ruins using a low center frequency UWB radar. In: Electromagnetic Research Symposium; 8–11 August 2016; Shanghai, China. New York, NY, USA: IEEE. pp. 1744-1747.

[16] Wu S, Yao S, Liu W, Tan K, Xia Z, Meng S, Chen J, Fang G, Yin H. Study on a novel UWB linear array human respiration model and detection method. IEEE J Sel Top Appl; 9: 125-140.

[17] Sakamoto T. Fast imaging method for security systems using ultrawideband radar. IEEE T Aero Elec Sys 2016; 52: 658-670.

[18] Hozhabri M, Risman PO, Petrovic N. Study of the environment effect by M-sequence UWB radar on detection of a walking human. In: IEEE Conference on Antenna Measurements & Applications; 23–27 October 2016; Syracuse, NY, USA. New York, NY, USA: IEEE. pp. 1-4.

[19] Hozhabri M, Otterskog M, Petrovic N, Ekstrom M. Experimental comparison study of UWB technologies for static human detection. In: IEEE International Conference on Ubiquitous Wireless Broadband; 16–19 October 2016; Nanjing, China. New York, NY, USA: IEEE. pp. 1-4.

[20] Valmori F, Giorgetti A, Mazzotti M, Paolini E, Chiani M. Indoor detection and tracking of human targets with UWB radar sensor networks In: IEEE International Conference on Ubiquitous Wireless Broadband; 16–19 October 2016; Nanjing, China. New York, NY, USA: IEEE. pp. 1-4.

[21] Lu Q, Liu C, Zeng Z, Li J, Zhang X. Detection of human's motions through a wall using UWB radar. In: 6th International Conference on Ground Penetrating Radar (GPR); 13–16 June 2016; Hong Kong. New York, NY, USA: IEEE. pp. 1-4.

[22] Bharadwaj R, Parini C, Alomainy A. Experimental investigation of 3-D human body localization using wearable ultra-wideband antennas. IEEE T Antenn Propag 2015; 63: 5035-5044.

[23] Salman R, Norrdine A, Damyanov D, Schultze T, Willms I, Blankenbach J. Accurate 3D UWB radar super-resolution imaging for a bi-static antenna configuration. In: International Conference on 3D Imaging; 14–15 December 2015; Liège, Belgium. New York, NY, USA: IEEE. pp. 1-6.

[24] Huang Q, Qu L, Wu B, Fang G. UWB through-wall imaging based on compressive sensing. IEEE T Geosci Remote 2010; 48: 1408-1415.

[25] Yanhui Z, Bei Z, Wenbo S, Tao W. Experimental research on relationships between dielectric constant of cement concrete materials and measuring frequency. In: 14th International Conference on Ground Penetrating Radar (GPR); 4–8 June 2012; Shanghai, China. New York, NY, USA: IEEE. pp. 403-406.